



Effects of millimetric geometric features on dropwise condensation under different vapor conditions

Yajing Zhao¹, Daniel J. Preston¹, Zhengmao Lu, Lenan Zhang, John Queeney, Evelyn N. Wang^{*}

Department of Mechanical Engineering, Massachusetts Institute of Technology, Cambridge, MA 02139, USA

ARTICLE INFO

Article history:

Received 26 July 2017

Received in revised form 20 November 2017

Accepted 27 November 2017

Keywords:

Dropwise condensation
Non-condensable gases
Geometric features
Heat transfer

ABSTRACT

In this work, we investigated the effects of millimetric surface structures on dropwise condensation heat transfer under two different environments: pure vapor and an air-vapor mixture. Our experimental results show that, although convex structures enable faster droplet growth in an air-vapor mixture, the same structures impose the opposite effect during pure vapor condensation, hindering droplet growth. We developed a model for each case to predict the heat flux distribution along the structured surface, and the model shows reasonable agreement with experimental results. This work demonstrates that the effects of geometric features on dropwise condensation are not invariable but rather dependent on the scenario of resistances to heat and mass transfer in the system. The fundamental understanding developed in this study provides useful guidelines for condensation applications including power generation, desalination, dew harvesting, and thermal management.

© 2017 Elsevier Ltd. All rights reserved.

1. Introduction

Condensation is a useful approach for energy transport due to the large amount of latent heat released during the phase change process. Condensation of water vapor has been routinely observed in nature [1–3] and commonly utilized in a wide range of applications such as desalination systems [4,5], steam cycles [6,7], water harvesting [8,9], and nuclear reactors [1–3,10,11]. In these applications, enhancement of the condensation heat and mass transfer performance can significantly contribute to energy efficiency, economic performance, and environmental sustainability of the overall system. Filmwise condensation is standard in industrial applications due to the high surface energy of common condenser materials, but this mode of condensation suffers from its intrinsic barrier to heat transfer created by the condensed liquid film. On the other hand, dropwise condensation, which has been demonstrated to exhibit 5–7 times higher heat transfer coefficients compared to filmwise condensation [12], has attracted much research interest since its discovery in 1930 [13].

The performance enhancement obtained by dropwise condensation is due to the gravity-induced removal of discrete droplets upon growing to a critical size near the capillary length, allowing renucleation and growth of small droplets; therefore, facilitating

droplet growth plays a critical role in dropwise condensation. As such, droplet growth has been studied at great length, both theoretically and experimentally. An early dropwise condensation theory combined the heat transfer rate through a single drop with the expression for drop size distribution to obtain the condensation heat flux on the surface [14]. Following this work, more advanced models have been developed by considering precise descriptions for droplet size distribution [15] and the effect of large contact angles [16,17]. Among experimental studies, a variety of micro- and nanoscale surface structures have been used to manipulate droplet growth. High droplet mobility and rapid droplet removal have been demonstrated on nanowires [18], nanocones [19], and hierarchical structures [20]. In addition, spatial control of microdroplets has been achieved on micro-pillar arrays [21], mesh-screen structures [22], and hybrid surfaces [23]. Furthermore, superhydrophobic nanotextured copper oxide surfaces [24–26] have been developed to enable micrometer-sized droplets to jump off of a surface regardless of gravity, which yields a higher condensation heat transfer coefficient compared with state-of-the-art dropwise condensing surfaces [27–31].

In contrast to micro- or nanoscale structures that require relatively intricate and costly manufacturing processes and are often prone to physical wear and destruction, recent studies have reported that millimeter-sized convex structures can effectively manipulate dropwise condensation. Park et al. [32] designed slippery asymmetric bumps which significantly facilitate droplet growth and departure and thereby show a sixfold-higher droplet

^{*} Corresponding author.

E-mail address: enwang@mit.edu (E.N. Wang).

¹ Indicates equal contribution.

Nomenclature

c	concentration (mol/m ³)
c_p	specific heat capacity (J/kg K)
D	diffusion coefficient (m ² /s)
h	heat transfer coefficient (W/(m ² K))
J	molecular diffusion rate (mol/s)
j	diffusion flux (mol/(m ² s))
k	thermal conductivity (W/(m·K))
P	pressure (Pa)
Q	heat transfer rate (W)
q	heat flux (W/m ²)
R_{th}	thermal resistance (m ² K/W)
T	temperature (K)

t	time (s)
-----	----------

Greek letters

δ	thickness (m)
ζ	diffusion boundary layer thickness (m)

Subscripts

b	bottom surface of the block
s	top surface of the block
∞	bulk state

growth rate compared to flat surfaces. Keeping track of droplet size distribution on the bumpy surface, they experimentally demonstrated that millimetric bumps alone can enhance condensation on the top of the bumps. Medici et al. [33] also studied the effect of millimeter-sized geometric features (corners, edges, grooves, and scratches) on droplet growth during condensation. They concluded that millimetric surface discontinuities can modify droplet growth rates such that droplets near outer corners and edges grow faster than those near inner corners, in agreement with Park's result. They also mentioned that this geometric effect disappears when condensing on a substrate with poor thermal conductivity. However, they attributed this phenomenon to the low thermal conductivity of the substrate material and did not consider the effects of the material property on the overall thermal resistance network, which is the critical aspect of the condensation profile.

Indeed, these two studies of millimeter-scale geometric effects on dropwise condensation are of great importance, since the condensation situation that is being considered there, i.e., vapor condensation in air, is ubiquitous in a variety of applications such as desalination [34], water harvesting [9], air cooling [35], and waste heat recovery [36]. However, these previous works did not take into account that the condensation performance is affected not only by geometric features but also by vapor conditions, i.e., the presence of non-condensable gases (air, in this case). Vapor condensation in the presence of non-condensable gases (NCGs) is hindered by the required vapor diffusion across a boundary layer introduced by NCG accumulation near the liquid-vapor interface [37–39]. It has been demonstrated that NCGs introduce additional heat and mass transfer resistance and therefore significantly degrade condensation performance in both the filmwise and dropwise modes [40]. In an early experimental demonstration of the filmwise mode [41], a decrease of nearly 50% in condensation heat transfer coefficient was observed in the presence of 0.5% NCG volume fraction. In accordance with this, a numerical study on laminar filmwise condensation [42] showed that the presence of a few percent of NCGs can substantially reduce condensation heat transfer and furthermore introduce a dramatic change in the temperature profile. The temperature of the liquid-vapor interface was calculated to be as high as the bulk vapor temperature in the absence of NCGs, but decreased to almost the cold wall temperature in the presence of 2% mass fraction of NCGs. A similar temperature profile altered by NCGs was observed in an experimental study where filmwise condensation with and without NCGs inside a vertical tube was investigated [43], and the authors attributed the altered temperature profile to the prominent influence of NCGs on the thermal resistance network. The wall temperature was observed to be close to the bulk vapor temperature in the pure-steam condensation mode because the gas side had negligible thermal resistance; however, it approached the coolant temperature

when the NCGs on the gas side dominated the overall thermal resistance network. This viewpoint of a NCG-influenced thermal resistance network was also explored in an experimental study [44] where the dropwise and the filmwise modes resulted in a similar range of heat transfer rates when condensing air-steam mixtures, owing to the governing role of the air-rich diffusion boundary layer in the thermal resistance network dominating that of the condensation modes.

Prior work has compared condensation heat transfer performance with and without NCGs [41–43,45], and recent work has shed light on geometrically enhanced dropwise condensation with NCGs [32,33], but geometric effects on dropwise condensation performance with and without NCGs have not been considered simultaneously. In the present study, we investigated the effects of millimetric geometric features on dropwise condensation under different vapor conditions by examining the heat transfer performance in two cases (air-vapor mixture vs. pure vapor). To provide an improved understanding of the physical phenomenon, we developed numerical models for both case studies based on analysis of the thermal resistance network involved in the heat and mass transfer process. The reasonable agreement between experimental results and modeling predictions demonstrates that the effect of geometric features on dropwise condensation is not absolute, but rather is determined by the specific thermal resistance scenario involved in the given case of heat and mass transfer, which can be completely altered by the presence of NCGs.

2. Materials and methods

2.1. Condensation substrate

A metal block 2.03 cm in width, 1.83 cm in height, and 2.11 cm in length, including a bump 0.38 cm in width, 0.38 cm in height, and 2.11 cm in length on the top surface, was milled to serve as the geometric-featured substrate for the present study (Fig. 1). In order to guarantee that heat would conduct from the top to the bottom surface of the block during condensation and to prevent condensation on the sidewalls, thermal insulation for the block sidewalls was provided with a 0.5 mm-thick polyetherimide (Ultem) frame snugly fit around the sides of the condensation block.

In order to demonstrate opposite condensation scenarios on the same substrate under the two vapor conditions (air-vapor mixture vs. pure vapor), we deliberately designed reverse thermal resistance scenarios under the two conditions by selecting titanium as the block material upon a preliminary thermal resistance analysis. The thermal resistance of the titanium block can be estimated using a simplified 1D conduction model by the following equation:

$$R_{th} = \delta/k \quad (1)$$

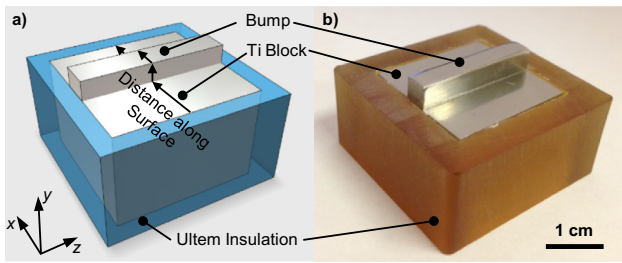


Fig. 1. A titanium block including a rectangular bump on the top surface was milled to serve as the condenser surface. The block was thermally insulated by polyetherimide. The schematic and a photo of the condenser surface with surrounding insulation are shown in (a) and (b), respectively.

where δ denotes the characteristic thickness of the geometric feature in the conduction direction (0.38 cm) and k is the thermal conductivity of the block material (for titanium, $k = 15.6 \text{ W}/(\text{m}\cdot\text{K})$). Consequently, the thermal resistance of the condensation block is on the order of $10^{-4} \text{ m}^2 \text{ K}/\text{W}$, almost 2 orders of magnitude between the characteristic thermal resistances of condensation in pure vapor and condensation in an air-vapor mixture, which can be estimated by the following equation:

$$R_{\text{th}} = 1/h \quad (2)$$

where h is the condensation heat transfer coefficient ($1/h$ is on the order of 10^{-6} – $10^{-5} \text{ m}^2 \text{ K}/\text{W}$ for pure vapor and 10^{-2} – $10^{-1} \text{ m}^2 \text{ K}/\text{W}$ for the air-vapor mixture) [6,12,34,36,46].

In order to achieve dropwise condensation, the titanium block was functionalized by depositing a fluorinated silane (trichloro (1H,1H,2H,2H-perfluorooctyl)-silane, Sigma-Aldrich) in the vapor phase. This coating yields an advancing contact angle of $\theta_a \approx 120.2 \pm 3.1^\circ$ measured on the flat surface of the sample, which is in good agreement with previous studies [19,27,47].

2.2. Experimental setup

We tested the heat transfer performance of the condensation block under two vapor conditions (air-vapor mixture vs. pure vapor) in a controlled condensation chamber (supplementary material, section S1) in which the total pressure can be accurately measured. The schematic (not to scale) and the images taken from the outside and the inside of the condensation chamber for the experimental setup are shown in Fig. 2(a), (b), and (c), respectively. Pure vapor was supplied from a heated water reservoir to the chamber. Vapor condensation took place on the top surface of the horizontally-placed condensation block, where droplets grew

without removal of condensate due to the absence of gravitational body forces parallel to the surface. The titanium condensation block was cooled down by a $2.54 \text{ cm} \times 2.54 \text{ cm} \times 1.27 \text{ cm}$ copper block cooling stage through a thin layer of double sided copper tape. Just beneath the copper tape, a small groove was carved on the cooling stage surface from its center to the midpoint of one of its edges, in which a J-type thermocouple was tightly embedded to monitor the local temperature. Considering the low thickness (0.09 mm) and the high conductivity ($\geq 5 \text{ W}/(\text{m}\cdot\text{K})$) of the copper type, the thermal resistance of the copper tape, which could be estimated as $R_{\text{th,copper tape}} = \delta_{\text{copper tape}}/k_{\text{copper tape}} \leq 1.8 \times 10^{-6} \text{ m}^2 \text{ K}/\text{W}$, is much less than the thermal resistance of the titanium block (on the order of $10^{-4} \text{ m}^2 \text{ K}/\text{W}$). Therefore, the temperature drop through the copper tape could be neglected, and it is justifiable to regard the measurement from the center thermocouple as the bottom surface temperature of the titanium block, T_b . A 6.35 mm diameter hole was drilled through the cooling stage, into which a copper cooling tube with the same outside diameter was inserted for internal chiller water flow. Visualization of the condensation development was achieved through a viewing window on the chamber, where a digital SLR camera (EOS Rebel T3, Canon) was placed in line with the viewing window. A mirror tilted at an angle of 45° was fixed above the condensation block to reflect an image of the top surface of the block for the camera to capture both the sidewall and the top surface of the bump. For the air-vapor mixture condensation experiment, both dry bulb temperature and wet bulb temperature of the bulk air-vapor mixture were measured by J-type thermocouples suspended in the chamber. The relative humidity calculated by the measured dry bulb and wet bulb temperatures were compared with the reference value measured by a humidity meter (RH820, OMEGA) placed in the chamber. For the pure vapor condensation experiment, vacuum was achieved with a vacuum pump before introducing water vapor into the chamber. Chamber pressure was monitored by a pressure transducer (925 Micro Pirani, MKS) throughout the experiment. All experimental data were collected by a data acquisition system (9205 & 9213, National Instruments) interfaced to a computer.

2.3. Experimental procedures

A set of strict procedures was followed throughout the experiments. For both case studies (air-vapor mixture and pure vapor), the same preparatory steps including preheating the chamber, degassing the water vapor reservoir, and installing the test sample were followed, as detailed in the supplementary material, section S2.

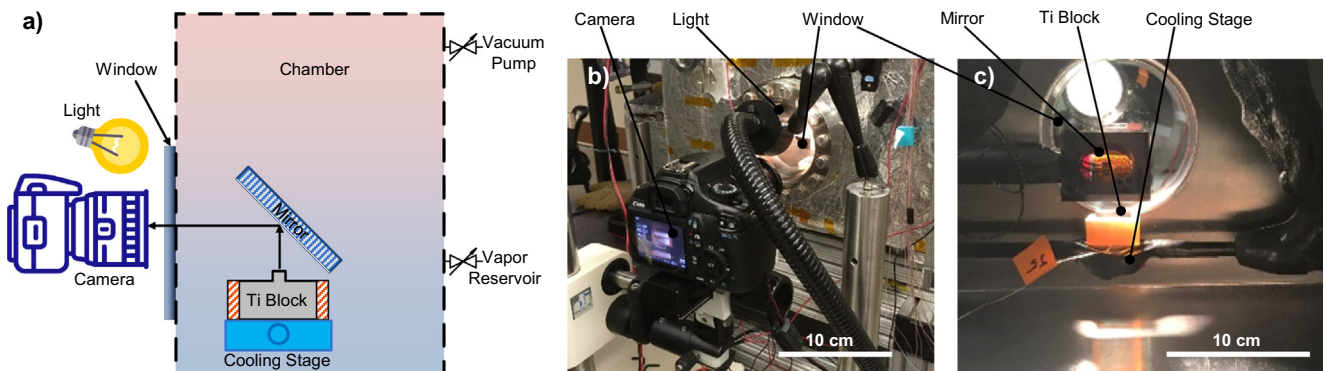


Fig. 2. The schematic (not to scale) and the images taken from the outside and the inside of the condensation chamber for the experimental setup are shown in (a), (b), and (c), respectively. The condensation block was horizontally placed on a cooling stage fixed in a controlled chamber. Water vapor was introduced from a reservoir into the chamber and condensed on the top surface of the block. A mirror tilted at 45° was used to reflect the top surface of the block to the camera outside the viewing window for visually recording data. Illumination was provided by a light source.

Both the experiments (air-vapor mixture condensation and pure vapor condensation) were carried out in the condensation chamber with the chamber door closed. The difference between these two experiments is the control over the vapor condition (i.e., the content of NCGs). In the air-vapor mixture case, the bellows valve connecting the inside of the chamber to the outside ambient was kept open in order to maintain an ambient pressure inside the chamber with inlet air. In the pure vapor case, the bellows valve was kept closed throughout the experiment, and the condensation chamber was evacuated to a vacuum of $P < 1.0$ Pa to eliminate NCGs prior to introducing the pure vapor from the reservoir. This vacuum condition was reached by following a standard pump-down procedure. First, the liquid nitrogen cold trap was filled to about half capacity. The ambient exposed valve connecting the chamber and the vacuum pump was closed and the valve connected to the liquid nitrogen cold trap was opened. Then, the vacuum pump was turned on, starting the pump-down process, during which the chamber pressure was continuously monitored. Typically, satisfactory vacuum conditions ($0.5 \text{ Pa} < P < 1 \text{ Pa}$) were reached after one hour of the pump-down process.

After the vapor condition was satisfied in each case (air-vapor mixture vs. pure vapor), the heater around the water vapor reservoir was turned down to 5% power and the vapor inflow valve was slowly opened until the operating conditions were achieved. Simultaneously, the camera was turned on to record condensation. A light source (KL 2500 LCD, SCHOTT) was fixed next to the camera outside the viewing window of the chamber for illumination. It took about two minutes of full operation to achieve steady state performance. For the air-vapor mixture case, the steady state condition was obtained at a bulk fluid temperature of $56 \text{ }^\circ\text{C}$ with a relative humidity of 80%. For the pure vapor condensation experiment, a steady state at vapor pressure of 6 kPa was maintained, which is a typical operation pressure for power plant condensers [48,49].

2.4. Numerical modeling

In order to understand the experimental results, we modeled each of the environmental conditions explored in the present work. Numerical models for dropwise condensation in both the air-vapor mixture and in pure vapor were developed for comparison with experimental results based on the following assumptions:

- (1) Condensation occurred at a steady state.
- (2) Variations in temperature or vapor concentration in the z direction (Fig. 1) were negligible (2D model).
- (3) Adiabatic conditions (no heat transfer or mass transfer in the horizontal direction) were applied to the two vertical boundaries of the considered 2D region, which is justifiable for the symmetric situation where an array of the same geometric features is used.
- (4) In the case of air-vapor mixture condensation, the gas region represented the largest thermal resistance and therefore the condensation block could be treated as isothermal at the bottom surface temperature T_b . Mass transfer of water vapor occurred in a diffusion boundary layer where convection effects were negligible [50].
- (5) In the case of pure vapor condensation, the gas region had negligible thermal resistance compared with the solid region. Therefore, the vapor was assumed to be saturated homogeneously in the chamber (including at the liquid-vapor interface on the block) at the bulk temperature T_∞ .

Note that here we approximated the surface temperature of the block T_s to be equivalent to the bottom surface temperature of the block T_b in the air-vapor mixture case and to the

saturation temperature of the bulk vapor T_∞ in the pure vapor case, based on analysis of the thermal resistances. During the experiments, we used this approximation instead of measuring the surface temperature directly because adding thermocouples onto the block surface would affect the droplet growth rate measurement during the image processing work. Afterwards, this temperature approximation was validated by direct measurement of the surface temperature under similar experimental conditions, as detailed in the [supplemental material, section S5](#).

For the air-vapor mixture condensation, large amounts of NCGs accumulated near the condensation surface, forming a boundary layer within which mass diffusion of water vapor was driven by the concentration gradient of water vapor. For the present study, a boundary layer thickness $\zeta \approx 1 \text{ cm}$ was calculated ([supplemental material, section S3](#)), which is in a good agreement with previous studies [32,33]. The vapor diffusion within the boundary layer followed:

$$\frac{\partial c}{\partial t} + \vec{\nabla} \cdot \vec{j} = 0, \quad (3)$$

where the first term represents the variation of vapor concentration with time and was set as zero under assumption (1). \vec{j} is the diffusion flux of water vapor, which can be determined by Fick's law:

$$\vec{j} = -D \vec{\nabla} c, \quad (4)$$

where D is the diffusion coefficient of vapor in air, which is related to temperature and pressure. For simplicity, a constant value of $3.0 \times 10^{-5} \text{ m}^2/\text{s}$ was assigned to D [51] due to the small range of variation in temperature and pressure considered in the present study.

In order to solve the concentration profile of water vapor in the gas region, the following boundary conditions were applied: (i) c at the bottom of the gas region equaled to c_s , corresponding to the saturation state of water vapor at the top surface temperature of the condensation block T_s , which was approximated to be the same as T_b due to assumption (4); (ii) c beyond the diffusion boundary layer equaled to c_∞ , corresponding to the concentration of the bulk air-vapor mixture with temperature, total pressure, and relative humidity measured from the experiment; and (iii) the two vertical boundaries were adiabatic.

The complete vapor concentration profile in the gas region was solved through a finite element method (schematically shown in Fig. 3) by iterating until convergence. Once the concentration profile was determined, we derived the heat flux distribution along the top surface of the condensation block combining the mass flux distribution with density and latent heat of the water vapor.

For the pure vapor condensation, the water vapor had negligible thermal resistance compared to the titanium condensation block, as discussed in Section 2.1. Hence, we assumed that the top surface temperature of the block equaled to the saturation temperature of the bulk vapor and derived the temperature profile inside the condensation block using the conduction equation:

$$\rho c_p \frac{\partial T}{\partial t} + \vec{\nabla} \cdot \vec{q} = 0, \quad (5)$$

where the first term represents the variation of block temperature with time and was assigned to be zero under assumption (1). \vec{q} is the heat flux through the condensation block, which was calculated by Fourier's law:

$$\vec{q} = -k \vec{\nabla} T. \quad (6)$$

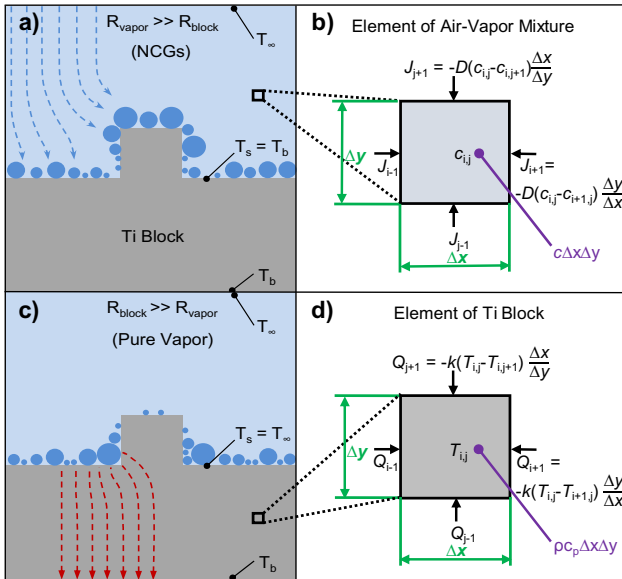


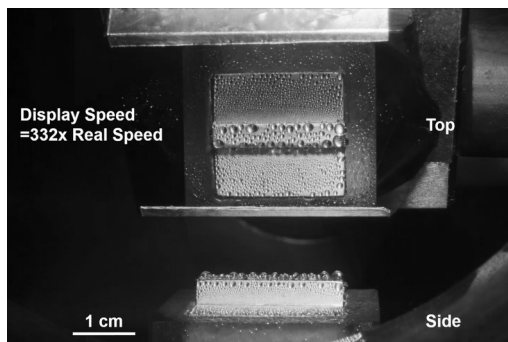
Fig. 3. Schematics of the numerical models for dropwise condensation with and without NCGs. For the air-vapor mixture case, the gas region dominates the thermal resistance; thus, T_s was equal to T_b and the concentration profile was determined by the diffusion equation, as illustrated by the boundary conditions and the governing equations shown in (a) and (b). For the pure vapor case, the solid region dominated the thermal resistance and thus T_s was equal to T_∞ and the concentration profile was determined by the conduction equation, as illustrated by the boundary conditions and the governing equations shown in (c) and (d).

In order to solve the temperature profile in the condensation block, the following boundary conditions were applied: (i) T at the bottom surface of the block equaled to the value measured from the experiment; (ii) T at the top surface of the block equaled to T_∞ , corresponding to the saturation temperature of the bulk vapor; and (iii) the two vertical boundaries were adiabatic.

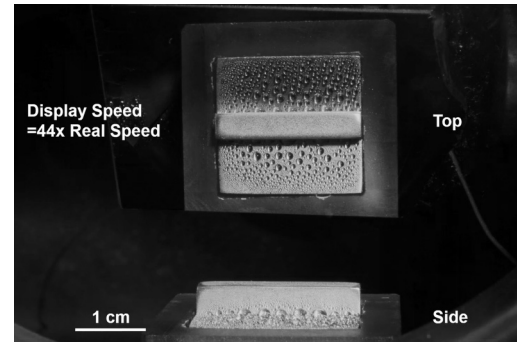
Similar to solving the vapor concentration profile in the gas region, the complete temperature profile of the condensation block was solved through a finite element method (schematically shown in Fig. 3) by iterating until convergence. Heat flux distribution along the top surface of the condensation block was then derived from the block temperature profile.

3. Results and discussion

Droplet growth on the top surface of the substrate was visually recorded throughout the condensation experiments (Supplementary movies 1 for air-vapor mixture condition and 2 for pure vapor condition).



Supplementary movie 1.



Supplementary movie 2.

Images of the condensation development on the substrate's top surface with air-vapor mixture and with pure vapor are shown in Fig. 4 (a) and (c), respectively. The upper images in the figures show the reflection of the block's top surface in the mirror, and the lower images show the sidewall of the bump. In both cases the substrate displayed dropwise condensation of water vapor, while the condensation rate and the droplet size distribution differed. When exposed to air, water vapor condensed mostly on the top surface of the bump, especially at the outer edges of the bump, but few condensed droplets were found in the inner corners of the bump, as shown in Fig. 4(a). This observation agrees with those from previous studies about geometric effects on dropwise condensation [14,15], demonstrating that the bumpy geometric feature provides local enhancement of dropwise condensation. However, in the pure vapor condensation experiment, the droplet size distribution pattern was reversed: vapor was observed to condense mostly at the inner corners of the bump, while little vapor condensed on the top surface of the bump, as shown in Fig. 4(c), which demonstrates that the bump has a local degradation effect on dropwise condensation. These results indicate that the same geometric feature (in this study, the bump) with the same material property can impose completely opposite effects on dropwise condensation under different vapor conditions (air-vapor mixture vs. pure vapor).

The condensation profile in the two case studies as discussed above could be determined by the concentration profile in the gas region (in the air-vapor mixture case) or the temperature profile in the solid region (in the pure vapor case), which was numerically solved based on the analysis of the thermal resistance network. The vapor concentration profile in the diffusion boundary layer for the air-vapor mixture case and the temperature profile in the condensation block for the pure vapor case, solved by the numerical models, are shown in Fig. 4(b) and (d), respectively. For the air-vapor mixture condensation, the largest thermal resistance existed in the gas region due to the presence of a large amount of NCGs. Hence, the bottom boundary of the gas region just above the condensation block was treated as isothermal at T_b , and the water vapor concentration there was fixed as a constant corresponding to the saturation condition. The condensation profile could be determined from vapor diffusion driven by the concentration gradient in the gas region. As a result, vapor preferably condensed on the outer edges of the bump where the vapor concentration gradient reached its maximum value. In contrast to the case of the air-vapor mixture condensation, in the pure vapor condensation experiment, pure vapor had a negligible thermal resistance compared to the condensation substrate. Thus, the upper boundary of the solid region just below the water vapor was treated as isothermal at T_∞ , and the condensation profile could be determined from the heat conduction driven by the temperature gradient in the solid region. Consequently, in the pure vapor case, vapor condensation was most likely to occur at the inner

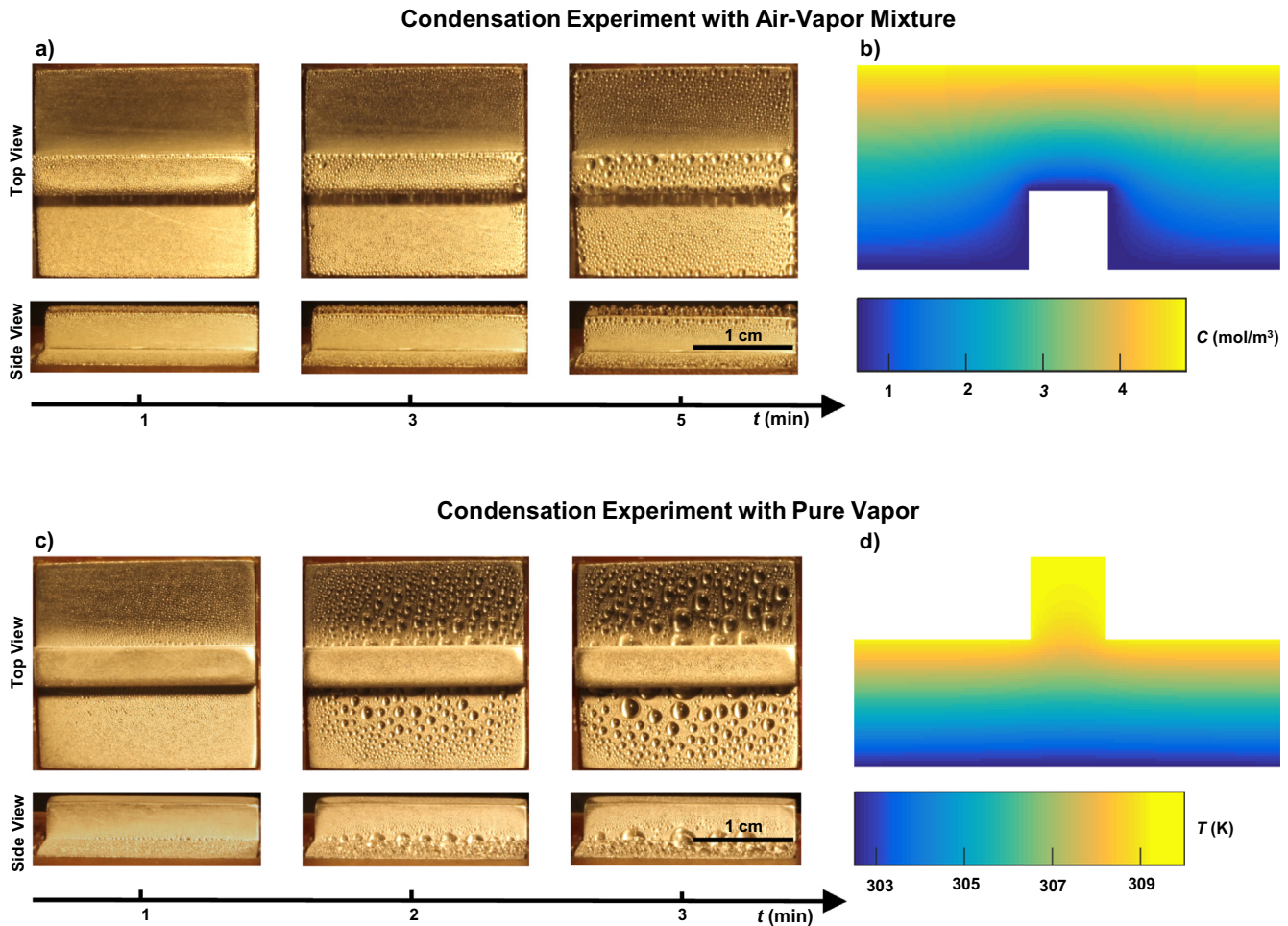


Fig. 4. Condensation profile of two case studies (air-vapor mixture vs. pure vapor). (a) Time-lapsed photographs of condensation development on the bumpy condensation substrate in the presence of air. (b) Numerical calculation of concentration profile in the air-vapor diffusion boundary layer for the case of air-vapor mixture condensation. (c) Time-lapse photographs of condensation development on the bumpy condensation substrate with pure vapor. (d) Numerical calculation of temperature profile in the condensation block for the case of pure vapor condensation.

corners of the bump where the temperature gradient reached its maximum value.

In order to quantify the condensation heat transfer performance in the experiments and to compare it with numerical modeling results, the heat flux distribution along the top surface of the condensation substrate was extracted from experimental data through image processing. Images for droplet growth development were continuously captured every 5 s for over 1000 s after condensation reached a steady state. The condensate mass increased almost linearly with time for the early stage of dropwise condensation where droplet coalescence did not significantly impact the heat transfer performance [35]. Thus, the condensation rate (mass per unit time) on the condensation substrate was reasonably obtained by dividing the total condensate mass difference between two selected times (within the early stage) by the time interval. In order to distinguish local heat transfer performance, the surface area of the top surface of the condensation block (in the images) was evenly divided into several regions within which heat flux could be obtained from condensation rate. Our image processing methodology along with the droplet size distribution data are detailed in the [supplementary material, section S4 and table S1](#).

Fig. 5(a) and (b) quantitatively show the condensation heat flux distribution along the top surface of the condensation block during the condensation experiments with the air-vapor mixture and with pure vapor, respectively. The black data points were extracted from the images obtained during the two experiments by image pro-

cessing. The blue solid lines show the heat flux distribution obtained from the numerical model. In the air-vapor mixture case, the maximum heat flux was reached at the outer edges of the bump, and there was little heat flux at the inner corners, as shown in Fig. 5(a). However, in the pure vapor case, the outer edges had almost no heat flux, and the maximum heat flux was reached at the inner corners, as shown in Fig. 5(b). The completely different heat flux distribution in the two cases is mainly due to the different thermal resistance network altered by the presence of NCGs, as discussed. In both case studies, the experimental data and the modeling results show reasonable agreement with each other, especially the good agreement in the bump region and the similar trends in heat flux distribution. The discrepancy occurring at the flat regions was mainly due to the fact that in our experiments, we only used one bump and there was inevitable heat/mass dissipation on the vertical boundaries of the solid/gas regions, which differs from the assumption (3) we used in our model. Adding a heat flux dissipation term into the heat transfer equation in the pure vapor case model, or adding a mass flux dissipation term into the mass transfer equation in the air-vapor mixture case model, would mitigate this difference between the modeling and the experimental results. However, the focus of the current numerical modeling work is to build a general model to illustrate the effects of geometric features on condensation heat transfer under different vapor conditions. Modeling the heat dissipations from the boundaries could deviate from the focus of the current study.

Therefore, we did not revise the model to compensate for the inevitable heat dissipation that occurred in the experiments. Despite the discrepancy in the flat regions, the reasonable agreement in heat flux distribution profile between experimental and modeling results demonstrates that the effects of the geometric features on dropwise condensation are not only determined by the geometric features themselves, but also significantly influenced by the vapor condition, which is capable of completely altering the thermal resistance network involved in the heat and mass transfer process. Based on our understanding, the condensation profile is determined by the overall thermal resistance network which is affected by many factors including the geometry of the condensation substrate, the material of the condensation substrate, and the vapor condition, rather than dependent on any one of these factors alone.

It is also worth noting that the heat flux obtained in the pure vapor condensation was generally much higher than the one obtained in the air-vapor mixture condensation. Averaging the local heat flux data along the block surface gave an average heat flux of $401 \pm 20 \text{ W/m}^2$ for the air-vapor mixture case study and $8676 \pm 551 \text{ W/m}^2$ for the pure vapor case study. Direct comparison between the two heat flux values is not meaningful since they were measured at different degrees of subcooling, $\Delta T = (T_\infty - T_s)$. However, seeing that the heat flux value in the pure vapor case was over 20 times larger than that in the air-vapor mixture case,

and that the subcooling in the pure vapor case was maintained at almost 0°C which was much smaller than that in the air-vapor mixture case, from a scaling perspective, we can infer that the heat transfer coefficient, which is the ratio of the heat flux to the subcooling, has a much larger value in the pure vapor case than in the air-vapor mixture case. Therefore, the NCGs in the air-vapor mixture case significantly degraded condensation heat transfer.

Finally, this work mainly focused on two extreme situations where the thermal resistance network was dominated by one region (either the gas region or the solid region). This great contrast in thermal resistance of the two regions enabled us to approximate the region with negligible resistance to be isothermal (assumptions (4) and (5)) and simplified our numerical modeling. However, it is also useful to consider more complicated situations where some of the simplifications or assumptions are not valid anymore. For example, in the case where the thermal conductivity of the condensation substrate is so low that the thermal resistance of the substrate is comparable to that of the air-vapor mixture above the substrate, it is no longer feasible to approximate the substrate surface as isothermal. Nevertheless, it is still applicable to carry out a comprehensive thermal resistance analysis to obtain condensation profile, as long as careful consideration is taken into the energy balance among conduction heat flux of the substrate, latent heat flux released by condensation, and conduction heat flux of the air-vapor mixture (when convection is neglected). By comparing the thermal resistance of the gas region to that of the solid region, we derived a dimensionless number:

$$N = \frac{k_{\text{solid}}}{k_{\text{gas}} + \frac{DMh_{\text{fg}}\Delta c}{\Delta T}} \quad (7)$$

to determine the condensation profile in general air-vapor mixture cases, where k , D , M , h_{fg} , c , and T represent thermal conductivity, diffusion coefficient of vapor in air, molar mass of water vapor, latent heat, concentration, and temperature, respectively. If $N \gg 1$, water vapor would preferably condense on the outer edges of geometric features; if $N \ll 1$, condensation would more likely happen at the inner corners of the features. Note that this dimensionless number is not applicable to the case of pure vapor condensation since Fick's law is not valid for transport of concentrated species. Detailed derivation of the dimensionless number N and its application to an extended case study with more complicated thermal resistance scenarios are discussed in the [supplementary material, section S6](#).

4. Conclusion

We investigated geometric effects on dropwise condensation, both with and without the presence of NCGs. Based on the analysis of the thermal resistance network, numerical models were developed for condensation heat flux distribution in the two cases. Meanwhile, droplet growth rate was experimentally captured and converted to heat flux through image processing. The reasonable agreement between modeling and experimental results demonstrates that the same convex geometric feature, or bump, can impose opposite effects on dropwise condensation in different vapor conditions. Based on our analysis, the effects of geometric features on dropwise condensation are not absolute, but rather depend on the thermal resistances involved in the system. The understanding gained in this study is expected to provide useful guidelines for related condensation applications such as dew harvesting, desalination, and air cooling.

Conflict of interest

None.

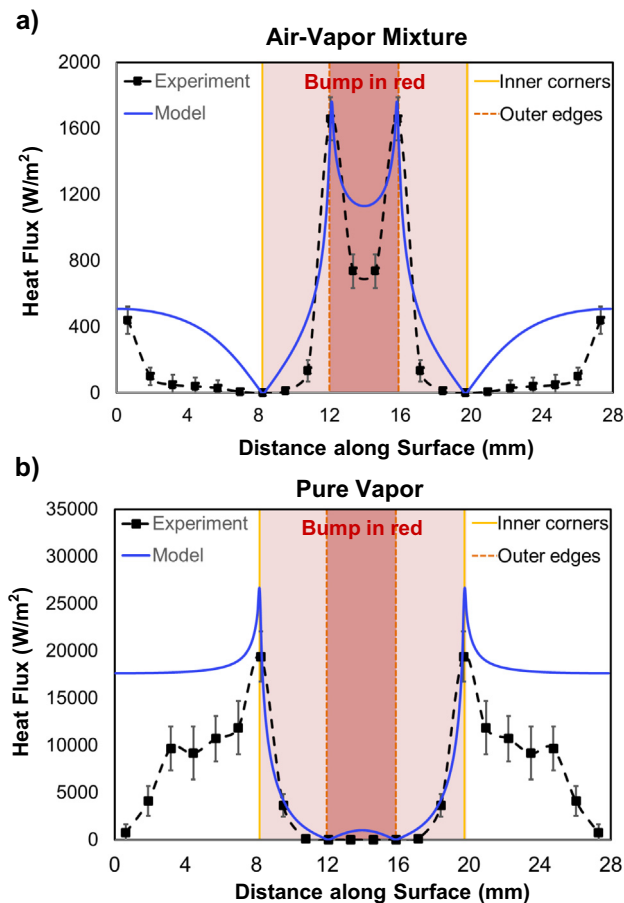


Fig. 5. Condensation heat flux distribution along the top condenser surface in two cases: (a) condensation with an air-vapor mixture, and (b) condensation with pure vapor. The bump region is highlighted in red with deep red for the top-surface region and light red for the sidewall region. Black data points are extracted from image processing on photographs taken from the experiments. Heat flux distribution derived from the numerical model is shown by the blue solid line. (For interpretation of the references to colour in this figure legend, the reader is referred to the web version of this article.)

Acknowledgements

The authors gratefully acknowledge funding support from the Abu Dhabi National Oil Company (ADNOC). The authors also gratefully acknowledge funding support from the Office of Naval Research (ONR) with Dr. Mark Spector as program manager. D. J. Preston acknowledges funding received by the National Science Foundation Graduate Research Fellowship under Grant No. 1122374. Any opinion, findings, conclusions, or recommendations expressed in this material are those of the author(s) and do not necessarily reflect the views of the National Science Foundation. Z. Lu acknowledges funding support from the Air Force Office of Scientific Research with Dr. Ali Sayir as program manager. L. Zhang acknowledges funding support from the MIT/MTL GaN Energy Initiative and the Singapore-MIT Alliance for Research and Technology (SMART) LEES program.

Appendix A. Supplementary material

Supplementary data associated with this article can be found, in the online version, at <https://doi.org/10.1016/j.ijheatmasstransfer.2017.11.139>.

References

- [1] C. Hao, Y. Liu, X. Chen, J. Li, M. Zhang, Y. Zhao, Z. Wang, Bioinspired interfacial materials with enhanced drop mobility: from fundamentals to multifunctional applications, *Small* 12 (14) (2016) 1825–1839.
- [2] Z. Huang, Y. Hwang, R. Radermacher, Review of nature-inspired heat exchanger, *Int. J. Refrig.* 78 (2017) 1–17.
- [3] H.J. Cho, D.J. Preston, Y. Zhu, E.N. Wang, Nanoengineered materials for liquid–vapour phase-change heat transfer, *Nat. Rev. Mater.* 2 (2016) 16092.
- [4] V.G. Rifert, A.I. Sardak, S.V. Grigorenko, V.I. Podbereznyj, Heat-exchange at dropwise condensation in heat-exchangers of desalination plants, *Desalination* 74 (1–3) (1989) 373–382.
- [5] G. Caruso, D. Vitale Di Maio, A. Naviglio, Condensation heat transfer coefficient with noncondensable gases inside near horizontal tubes, *Desalination* 309 (2013) 247–253.
- [6] D.J. Preston, D.L. Mafra, N. Miljkovic, J. Kong, E.N. Wang, Scalable graphene coatings for enhanced condensation heat transfer, *Nano Lett.* 15 (5) (2015) 2902–2909.
- [7] B.M.B.G.C. D.A. McNeil, Dropwise condensation of steam on a small tube bundle at turbine condenser conditions, *Exp. Heat Transfer* 13(2) (2000) 89–105.
- [8] K.C. Park, S.S. Chhatre, S. Srinivasan, R.E. Cohen, G.H. McKinley, Optimal design of permeable fiber network structures for fog harvesting, *Langmuir* 29 (43) (2013) 13269–13277.
- [9] H. Kim, S. Yang, S.R. Rao, S. Narayanan, E.A. Kapustin, H. Furukawa, A.S. Umans, O.M. Yaghi, E.N. Wang, Water harvesting from air with metal-organic frameworks powered by natural sunlight, *Science* 356 (6336) (2017) 430–434.
- [10] M.K. Yadav, S. Khandekar, P.K. Sharma, An integrated approach to steam condensation studies inside reactor containments: a review, *Nucl. Eng. Des.* 300 (2016) 181–209.
- [11] H. Kim, T.-S. Kwon, D.E. Kim, Experimental study of air-cooled water condensation in slightly inclined circular tube using infrared temperature measurement technique, *Nucl. Eng. Des.* 308 (2016) 38–50.
- [12] J.W. Rose, dropwise condensation theory and experiment: a review, *Proc. Inst. Mech. Eng.* 216 (2002) 115–128.
- [13] E. Schmidt, W. Schurig, W. Sellschopp, Versuche über die Kondensation von Wasserdampf in Film- und Tropfenform, *Tech. Mech. Thermodynam.* 1 (1930) 53–63.
- [14] E.J. Le Fevre, J.W. Rose, A theory of heat transfer by dropwise condensation, in: *Proc. Third Int. Heat Transfer Conf.*, 1966, pp. 362–375.
- [15] H. Tanaka, A theoretical study of dropwise condensation, *Trans. ASME J. Heat Transfer* 97 (1975) 72–78.
- [16] S. Kim, K.J. Kim, Dropwise condensation modeling suitable for superhydrophobic surfaces, *J. Heat Transfer* 133 (8) (2011) 081502.
- [17] N. Miljkovic, R. Enright, E.N. Wang, Modeling and optimization of superhydrophobic condensation, *J. Heat Transfer* 135 (11) (2013), 111004.
- [18] R. Wen, Q. Li, J. Wu, G. Wu, W. Wang, Y. Chen, X. Ma, D. Zhao, R. Yang, Hydrophobic copper nanowires for enhancing condensation heat transfer, *Nano Energy* 33 (2017) 177–183.
- [19] T. Mouterde, C. Lehoucq, S. Xavier, A. Checchio, C.T. Black, A. Rahman, T. Midavaine, C. Clanet, D. Quere, Antifogging abilities of model nanotextures, *Nat. Mater.* (2017).
- [20] C.-H. Chen, Q. Cai, C. Tsai, C.-L. Chen, G. Xiong, Y. Yu, Z. Ren, Dropwise condensation on superhydrophobic surfaces with two-tier roughness, *Appl. Phys. Lett.* 90 (17) (2007) 173108.
- [21] N.K. Mandsberg, R. Taboryski, Spatial control of condensation on chemically homogeneous pillar-built surfaces, *Langmuir* (2017).
- [22] J. Xie, J. Xu, X. He, Q. Liu, Large scale generation of micro-droplet array by vapor condensation on mesh screen piece, *Sci. Rep.* 7 (2017) 39932.
- [23] K.K. Varanasi, M. Hsu, N. Bhate, W. Yang, T. Deng, Spatial control in the heterogeneous nucleation of water, *Appl. Phys. Lett.* 95 (9) (2009) 094101.
- [24] D.J. Preston, A. Anders, B. Barabadi, E. Tio, Y. Zhu, D.A. Dai, E.N. Wang, Electrowetting-on-dielectric actuation of a vertical translation and angular manipulation stage, *Appl. Phys. Lett.* 109 (24) (2016) 244102.
- [25] Y. Nam, Y.S. Ju, Comparative study of copper oxidation schemes and their effects on surface wettability, in: *Imece 2008: Heat Transfer, Fluid Flows, and Thermal Systems*, Vol 10, Pts a-C, 2009, pp. 1833–1838.
- [26] N. Miljkovic, D.J. Preston, R. Enright, E.N. Wang, Jumping-droplet electrostatic energy harvesting, *Appl. Phys. Lett.* 105 (1) (2014).
- [27] N. Miljkovic, R. Enright, Y. Nam, K. Lopez, N. Dou, J. Sack, E.N. Wang, Jumping-droplet-enhanced condensation on scalable superhydrophobic nanostructured surfaces, *Nano Lett.* 13 (1) (2013) 179–187.
- [28] A. Cavalli, D.J. Preston, E. Tio, D.W. Martin, N. Miljkovic, E.N. Wang, F. Blanchette, J.W.M. Bush, Electrically induced drop detachment and ejection, *Phys. Fluids* 28 (2) (2016).
- [29] D.J. Preston, N. Miljkovic, R. Enright, E.N. Wang, Jumping droplet electrostatic charging and effect on vapor drag, *J. Heat. Trans.-T. Asme* 136 (8) (2014).
- [30] N. Miljkovic, D.J. Preston, R. Enright, E.N. Wang, Electrostatic charging of jumping droplets, *Nat. Commun.* 4 (2517) (2013).
- [31] J. Oh, P. Birbarah, T. Foulkes, S.L. Yin, M. Rentauskas, J. Neely, R.C.N. Pilawa-Podgurski, N. Miljkovic, Jumping-droplet electronics hot-spot cooling, *Appl. Phys. Lett.* 110 (12) (2017).
- [32] K.C. Park, P. Kim, A. Grinthal, N. He, D. Fox, J.C. Weaver, J. Aizenberg, Condensation on slippery asymmetric bumps, *Nature* 531 (7592) (2016) 78–82.
- [33] M.G. Medici, A. Mongruel, L. Royon, D. Beysens, Edge effects on water droplet condensation, *Phys. Rev. E Stat. Nonlin. Soft Matter Phys.* 90 (6) (2014) 062403.
- [34] A.M. Zhu, S.C. Wang, J.X. Sun, L.X. Xie, Z. Wang, Effects of high fractional noncondensable gas on condensation in the dewvaporation desalination process, *Desalination* 214 (1–3) (2007) 128–137.
- [35] S. Danilo, C. Dominique, P. Frederic, Experimental dropwise condensation of unsaturated humid air – influence of humidity level on latent and convective heat transfer for fully developed turbulent flow, *Int. J. Heat Mass Trans.* 102 (2016) 846–855.
- [36] C. Chantana, S. Kumar, Experimental and theoretical investigation of air-steam condensation in a vertical tube at low inlet steam fractions, *Appl. Therm. Eng.* 54 (2) (2013) 399–412.
- [37] A.P. Colburn, O.A. Hougen, Design of cooler condensers for mixtures of vapors with noncondensing gases, *Ind. Eng. Chem.* 26 (1934) 1178–1182.
- [38] W.J. Minkowycz, E.M. Sparrow, Condensation heat transfer in the presence of noncondensables, interfacial resistance, superheating, variable properties, and diffusion, *Int. J. Heat Mass Transf.* 9 (10) (1966) 1125–1144.
- [39] Y. Liao, K. Vierow, A generalized diffusion layer model for condensation of vapor with noncondensable gases, *J. Heat Transfer* 129 (8) (2007) 988.
- [40] J. Huang, J. Zhang, L. Wang, Review of vapor condensation heat and mass transfer in the presence of non-condensable gas, *Appl. Therm. Eng.* 89 (2015) 469–484.
- [41] F.F. Othmer, The condensation of steam, *Ind. Eng. Chem.* 21 (1929) 577–583.
- [42] E.M. Sparrow, E.R.G. Eckert, Effects of superheated vapor and noncondensable gases on laminar film condensation, *Aiche J.* 7 (3) (1961) 473–477.
- [43] S.B. Al-Shammari, D.R. Webb, P. Heggs, Condensation of steam with and without the presence of non-condensable gases in a vertical tube, *Desalination* 169 (2) (2004) 151–160.
- [44] C. Bum-Jin, K. Sin, K. Min Chan, M. Ahmadinejad, Experimental comparison of film-wise and drop-wise condensations of steam on vertical flat plates with the presence of air, *Int. Commun. Heat Mass Transfer* 31 (8) (2004) 1067–1074.
- [45] H.K. Al-Diwany, J.W. Rose, Free convection film condensation of steam in the presence of non-condensing gases, *Int. J. Heat Mass Transf.* 16 (1973) 1359–1369.
- [46] P. Götze, C. Philipp, U. Gross, Dropwise condensation experiments with humid air at a polymer surface, *J. Phys. Conf. Ser.* 395 (2012) 012129.
- [47] J.D. Smith, A.J. Meuler, H.L. Bralower, R. Venkatesan, S. Subramanian, R.E. Cohen, G.H. McKinley, K.K. Varanasi, Hydrate-phobic surfaces: fundamental studies in clathrate hydrate adhesion reduction, *Phys. Chem. Chem. Phys.* 14 (17) (2012) 6013–6020.
- [48] A. Vosough, A. Falahat, S. Vosough, H.N. Esfehiani, A. Behjat, R.N. Rad, Improvement power plant efficiency with condenser pressure, *Int. J. Multidiscipl. Sci. Eng.* 2 (2011) 38–43.
- [49] Y. Zhao, J. Wang, L. Cao, Y. Wang, Comprehensive analysis and parametric optimization of a CCP (combined cooling and power) system driven by geothermal source, *Energy* 97 (2016) 470–487.
- [50] D. Beysens, Dew nucleation and growth, *C.R. Phys.* 7 (9–10) (2006) 1082–1100.
- [51] A.F. Mills, *Mass Transfer*, first ed., Prentice Hall, 2001.

Supplementary Material for:

**Effects of Millimetric Geometric Features on Dropwise
Condensation under Different Vapor Conditions**

Yajing Zhao^{1†}, Daniel J Preston^{1†}, Zhengmao Lu¹, Lenan Zhang¹, John Queeney¹, and Evelyn N Wang^{1*}

¹*Department of Mechanical Engineering, Massachusetts Institute of Technology, Cambridge, Massachusetts 02139, USA*

[†]*Indicates equal contribution*

^{*}*Corresponding author email: enwang@mit.edu*

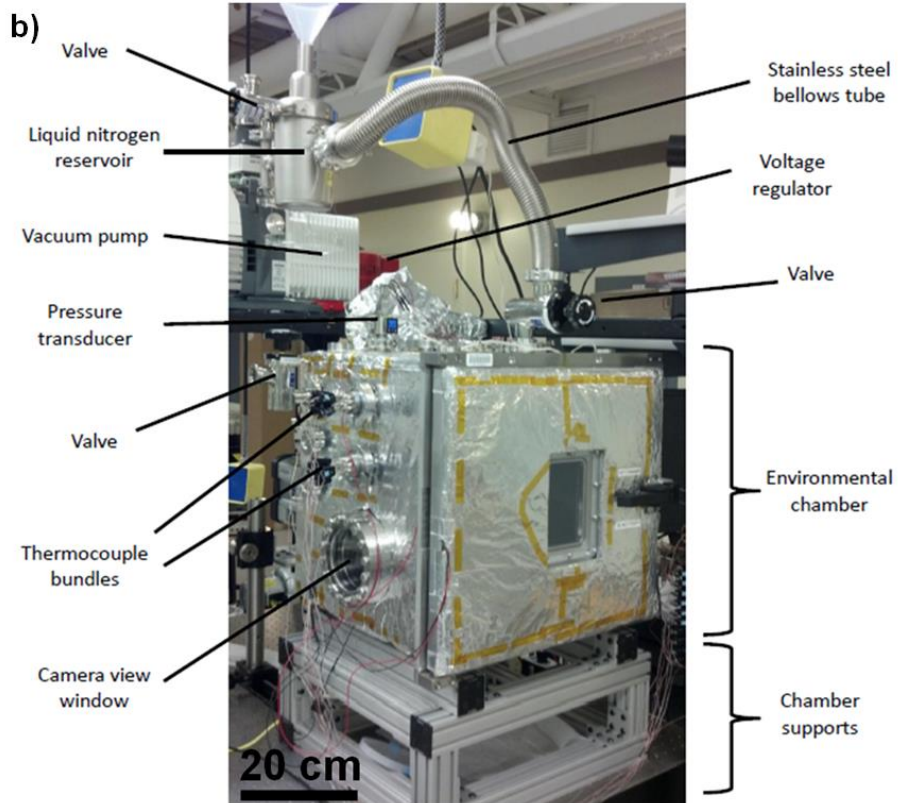
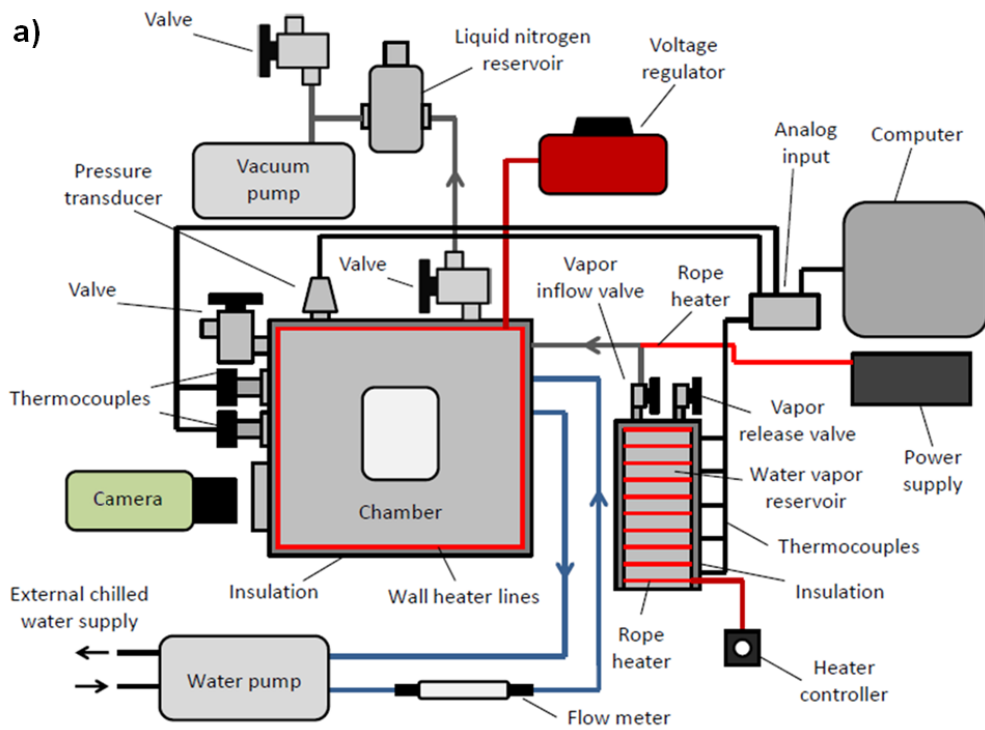
S1. Condensation chamber setup

The custom environmental chamber used for this work (Kurt J. Lesker) consists of a stainless steel frame with a door (sealed with a rubber gasket), two viewing windows, and apertures for various components. Resistive heater lines were wrapped around the exterior of the chamber walls to prevent condensation at the inside walls and then insulated on the exterior walls. The output power of the resistive heater lines was controlled by a voltage regulator (Variac). Two thermally insulated stainless steel water flow lines (Swagelok) were fed into the chamber *via* a KF flange port (Kurt J. Lesker) to supply cooling water to the chamber from a large capacity chiller (System III, Neslab). A flowmeter (7 LPM MAX, Hedland) with an accuracy of $\pm 2\%$ was integrated along the water inflow line.

A secondary stainless steel tube line was fed into the chamber *via* a KF adapter port that served as the flow line for the incoming water vapor supplied from a heated steel water reservoir. The vapor reservoir was wrapped with a rope heater (120 W, Omega) and thermally insulated to limit heat losses to the environment. The access tubes were welded to the vapor reservoir, each with independently-controlled valves. The first valve (Diaphragm Type, Swagelok), connecting the bottom of the reservoir to the ambient, was used to fill the reservoir with water. The second valve (BK-60, Swagelok), connecting the top of the reservoir to the inside of the chamber, provided a path for vapor inflow. K-type thermocouples were located along the length of the water vapor reservoir to monitor temperature.

A bellows valve (Kurt J. Lesker) was attached to the chamber to serve as a leak port between the ambient and inside of the chamber. In order to monitor temperatures within the chamber, J-type thermocouple bundles were connected through the chamber apertures *via* a thermocouple feed through (Kurt J. Lesker). A pressure transducer (925 Micro Pirani, MKS) was attached to monitor pressure within the chamber. The thermocouple bundles and the pressure transducer were both electrically connected to an analog input source (9205&9213, National Instruments), which was interfaced to a computer for data recording. A second bellows valve (Kurt J. Lesker) was integrated onto the chamber for the vacuum pump, which brought down the chamber to vacuum conditions prior to vapor filling. A liquid nitrogen cold trap was incorporated along the line from the chamber to the vacuum which served to remove any moisture from the pump-down process and ultimately assist in yielding higher quality vacuum

conditions. A tertiary bellows valve (Kurt J. Lesker) was integrated on a T fitting between the vacuum pump and liquid



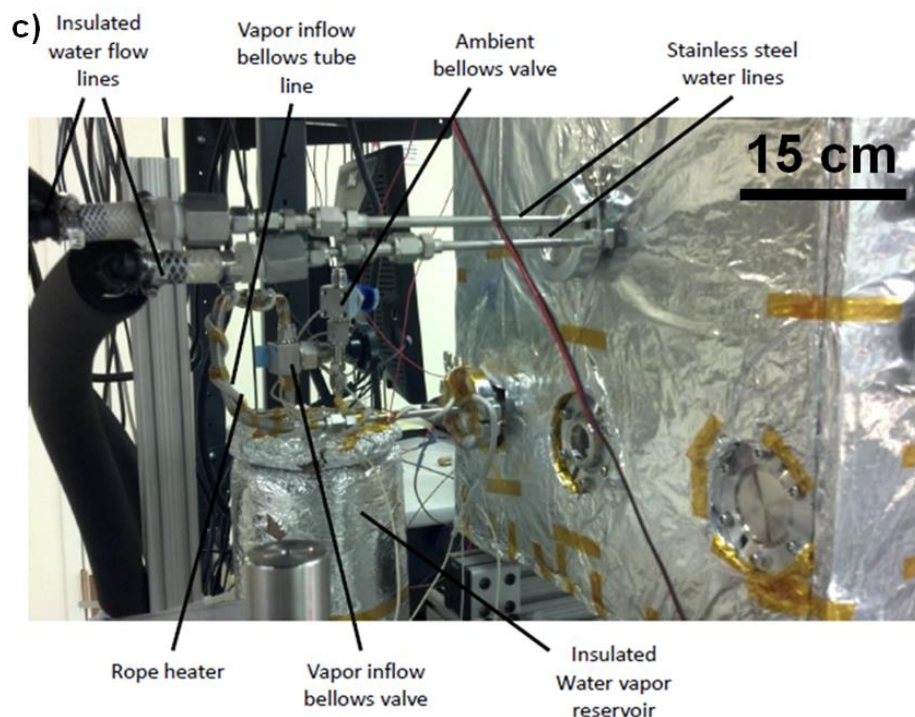


Figure S1. (a) Schematic of experimental setup (not to scale). (b) Image of the experimental setup shown from the front (camera and data acquisition system not shown). (c) Image of the experimental setup from the rear of the chamber showing the cooling water inlet and outlet and water vapor reservoir. Reprinted with permission from Reference 1. Copyright 2012 American Chemical Society.[1]

nitrogen reservoir to connect the vacuum line to the ambient to release the vacuum line to ambient conditions once pump down was achieved. In order to visually capture data, a digital SLR camera (EOS Rebel T3, Canon) was placed in line with the 5" viewing windows on the chamber. The schematic of the exterior of the environmental setup is depicted in Figure S1a. Images of the front and rear of the experimental setup are shown in Figures S1b and c, respectively.

S2. Experimental preparation

The first step was to turn on the voltage regulator to heat the condensation chamber walls up to a temperature over 35°C such that vapor would not condense on the chamber wall. Meanwhile, the water vapor reservoir was degassed through the following procedures. Initially, 3.5 liters of DI water (99% full) was filled into the reservoir using a syringe through a vapor release valve on the reservoir. Then, the vapor release valve was closed and a vapor inflow valve connecting the water vapor reservoir to the chamber was opened, when the rope heater around the reservoir was turned on with its maximum power (120 W). Two K type thermocouples were installed in the water vapor reservoir monitoring the temperature at the top and at the bottom section of the reservoir respectively. The top section temperature was measured to be higher than the bottom section temperature, because of the water thermal-mass present at the middle/bottom section. Thus, we ensured that the regions in the reservoir with higher thermal capacity were brought to a sufficiently high temperature for boiling. Once boiling occurred and both the top section temperature and the bottom section temperature of the reservoir were measured to be higher than 95°C for more than 10 minutes, the vapor inflow valve was closed. The excess water that spilled inside the chamber during the degassing process was removed.

In order to install the test sample onto the rig (Figure S1), the two ends of the copper cooling tube were connected to two 90-degree male elbow connectors on the rig. After all adapters/connectors were tightened without leaks that could influence vapor conditions, the bellow tubes were connected to the water lines for circulating cooling water and the test setup was placed onto the steel supports. Then, the mirror was fixed onto the steel supports facing towards the test sample with a tilting angle of 45° to reflect the top surface of the bumpy structure to the camera which was placed in line with the viewing window outside the chamber. All of the tubes for cooling water flow inside the chamber except the section inside the cooling stage were insulated and the mirror was attached to a heating pad (power 5W, 3M), in order to avoid vapor condensation on them.

S3. Boundary layer thickness approximation

The thickness of the diffusion boundary layer can be approximated using the method of shape factor, based on the analogy between the heat conduction problem and the mass diffusion problem described as follows. Consider a conduction heat transfer problem where a thin rectangular plate with length L and width W ($W > L$) at a uniform temperature T_1 is attached to a semi-infinite medium with a far-field temperature of T_2 , as shown in Figure S2.

At steady state and with a constant thermal conductivity of the rectangular plate, the governing equation for this heat transfer problem can be simplified as:

$$\frac{\partial^2 T}{\partial x^2} + \frac{\partial^2 T}{\partial y^2} + \frac{\partial^2 T}{\partial z^2} = 0 \quad (\text{S1})$$

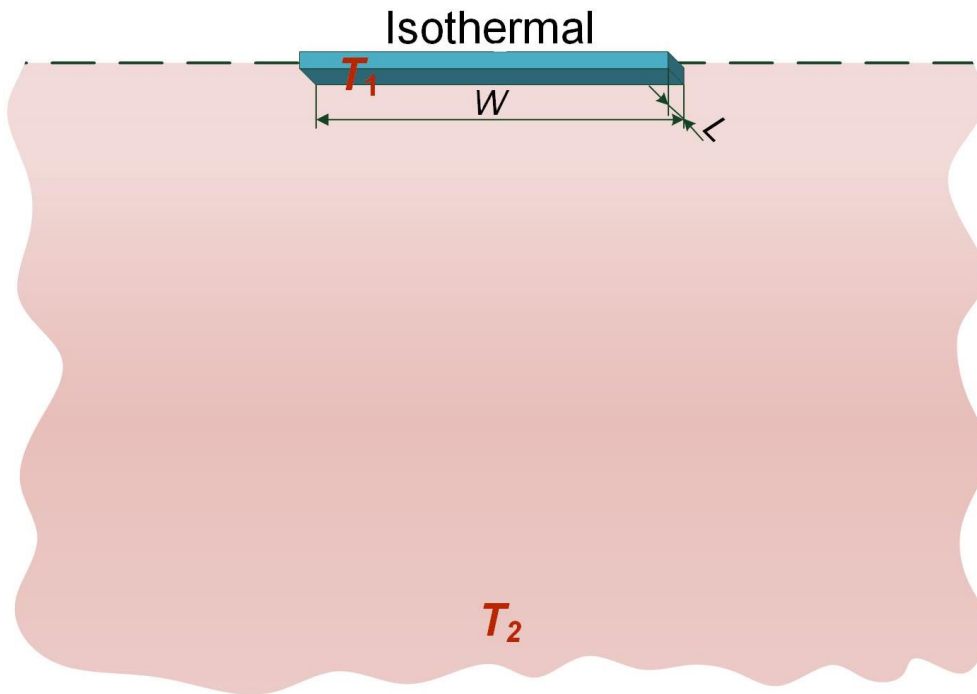


Figure S2. A thin rectangular plate of length L (into page), width W with a uniform temperature of T_1 attached to a semi-infinite medium having isothermal surface. The far-field temperature and the isothermal surface temperature for the semi-infinite medium are the same as T_2 .

In addition, two boundary conditions need to be satisfied:

$$T_{\text{plate}} = T_1; T_{\text{far-field}} = T_2. \quad (\text{S2})$$

Thereby, Equation (S1) along with boundary conditions (S2) completely describe the conduction heat transfer problem mentioned above.

For a steady-state conduction problem where heat is conducted between two isothermal surfaces (or objects), the conduction shape factor S is defined such that

$$\dot{Q} = kS\Delta T, \quad (\text{S3})$$

where \dot{Q} denotes the total amount of heat being conducted, k is the thermal conductivity of the material within which heat is transferred, and ΔT represents the temperature difference between the two isothermal surfaces (or objects).

For the case of a thin rectangular plate at T_1 exchanging heat with a semi-infinite medium at T_2 , as shown in Figure S2, the conduction shape factor has been given as [2]:

$$S = \frac{\pi W}{\ln(4W/L)}, (W > L). \quad (\text{S4})$$

Therefore, the total amount of heat being conducted can be calculated as:

$$\dot{Q} = kS\Delta T = \frac{\pi Wk\Delta T}{\ln(4W/L)}. \quad (\text{S5})$$

Now consider the mass diffusion problem in the case of air-vapor mixture condensation in the current study. Seeing that the bumpy geometric feature is small compared to the whole condensation block and that the condensation block can be treated as isothermal according to assumption (4), we can simplify the condensation block to a thin, 2.11 cm×2.03 cm plate with a

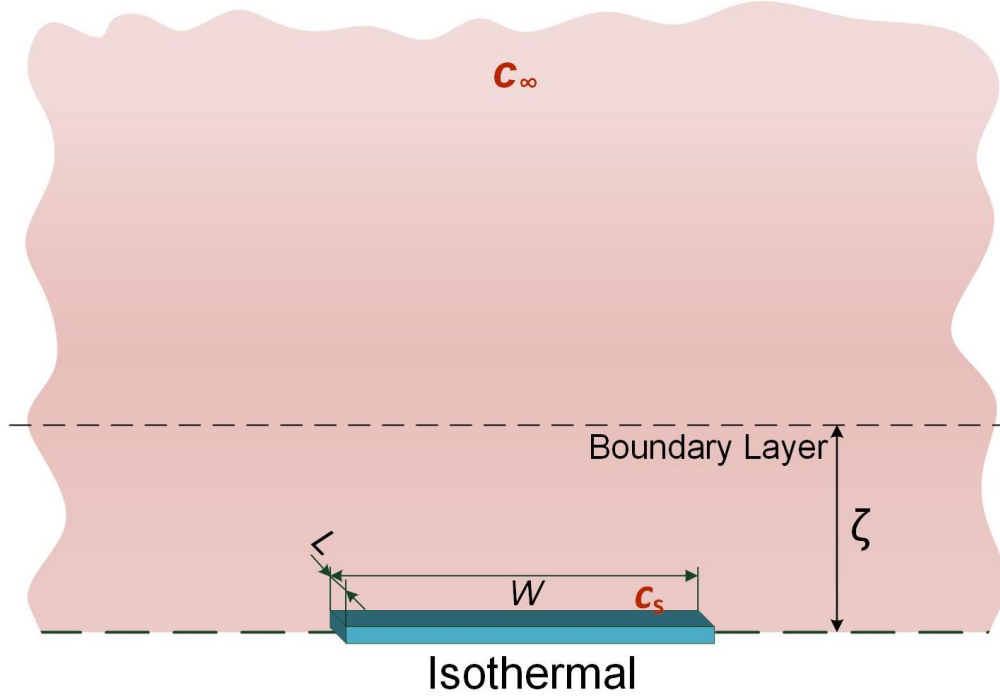


Figure S3. Simplified schematic for vapor condensation on the block in the presence of air. The block is simplified as a 2.11 cm×2.03 cm thin plate with a constant vapor concentration of c_s at its surface. The air-vapor mixture has a far-field vapor concentration of c_∞ . Mass transfer mainly occurs through vapor diffusion in a near-surface boundary layer of thickness ζ .

vapor concentration of c_s at its surface, being attached to a semi-infinite medium with a far-field vapor condensation of c_∞ .

A schematic for the diffusion problem is shown in Figure S3. At steady state and with a constant diffusion coefficient, the governing equation for this mass transfer problem can be simplified as:

$$\frac{\partial^2 c}{\partial x^2} + \frac{\partial^2 c}{\partial y^2} + \frac{\partial^2 c}{\partial z^2} = 0. \quad (\text{S6})$$

In addition, two boundary conditions need to be satisfied:

$$c_{\text{plate}} = c_s; c_{\text{far-field}} = c_\infty. \quad (\text{S7})$$

Equation (S6) and boundary conditions (S7) provide a complete description for the diffusion mass transfer problem.

From a comparison between the governing equations and boundary conditions for the conduction heat transfer problem and the diffusion mass transfer problem mentioned above, it is obvious that these two problems are analogous to each other in mathematics, and hence should have analogous forms of solutions. Therefore, it is reasonable to utilize the shape factor in the conduction problem to approximate the boundary layer thickness in the diffusion problem, as described below.

On the one hand, as an analogy to Equation (S5), the total vapor molecules being transferred per unit time through diffusion can be calculated as:

$$\dot{J} = DS\Delta c = \frac{\pi W D \Delta c}{\ln(4W / L)}. \quad (S8)$$

On the other hand, under the assumption that mass transfer mainly occurs within a diffusion boundary layer with thickness ζ [3, 4], the total vapor mass being transferred can be derived based on Fick's law:

$$\dot{J} = A \left(D \frac{\Delta c}{\zeta} \right) = (LW) \left(D \frac{\Delta c}{\zeta} \right), \quad (S9)$$

where A denotes the surface area of the plate and equals to the product of W and L .

Combining Equations (S8) and (S9) gives a diffusion boundary layer thickness of 0.92 cm. In the numerical modeling, we used 1 cm as the boundary layer thickness.

S4. Image processing methodology

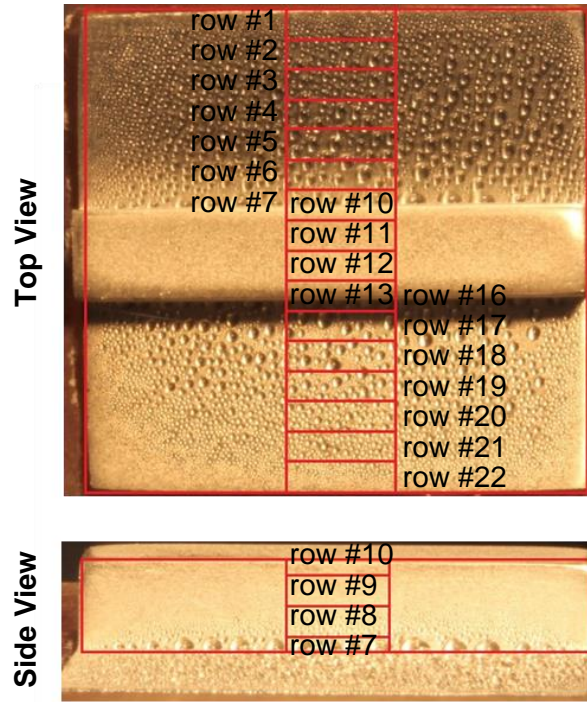


Figure S4. Division of the surface area of the condensation block's top surface in the photograph for condensation rate analysis.

In the experimental analysis, we derived the heat flux from droplet growth rate, which is a valid technique that has been frequently used in the literature [5-7]. For each case of the condensation experiments (i.e., air-vapor mixture or pure vapor), two photographs captured at different time points during the early stage of the steady state dropwise condensation were carefully selected for image processing. In order to distinguish the local heat transfer performance, the top surface of the condensation block in each photograph was evenly divided into 22 rows, as shown in Figure S4. For each row, the center 1/5 part was selected as the representative region for calculating condensation rate in that row. The reasons for this simplification include: (i) The variations in temperature in the z direction (Figure 1) were assumed to be negligible (2D model), thus ideally each column should have the same condensation rate; (ii) Heat loss to the insulation frame in z direction was inevitable in reality, and the center part experienced the least undesirable heat loss, as expected.

For each unit region, we used a pixel-counting software to measure the radius R of each droplet with diameter larger than 2 pixels and summed up their volume, which can be calculated by:

$$V_{\text{drop}} = \pi R^3 \left(\frac{2}{3} - \cos \theta + \frac{\cos^3 \theta}{3} \right), \quad (\text{S10})$$

where θ is the advancing contact angle. Then, the average heat flux in each row can be derived by integrating the condensation rate, the density and the latent heat of the water:

$$q = \frac{\sum V_{\text{drop},t+\Delta t} - \sum V_{\text{drop},t}}{A \cdot \Delta t} \cdot \rho \cdot h_{fg}, \quad (\text{S11})$$

where q is the average heat flux of one row, t denotes the time; A is the surface area of one row; ρ and h_{fg} represent the density and the latent heat of the water, respectively.

Due to symmetry, we obtained the heat flux in rows 12-22 by directly mirroring the data for rows 1-11 along the symmetrical line. Droplet size distribution data obtained from image processing are detailed in the attached excel file: table S1. Droplet size distribution. The image processing results are shown in Figure 5. Error bars indicate the propagation of error associated with the droplet diameter measurement (± 1 pixel) during the image processing.

S5. Validation of temperature profile through direct measurement

In the numerical modeling, based on thermal resistance analysis for the two cases, we made the approximation that the top surface temperature of the sample block T_s equaled to the bottom temperature of the block T_b in the air-vapor mixture case and to the saturation temperature of the bulk vapor T_∞ in the pure vapor case. We validated this approximation through direct temperature measurement for the two case studies.

In order to obtain the temperature profile on the top surface of the block, we attached three 36 gage (AWG, 0.13 mm in diameter) thermocouples at three different locations on the top surface of the block: (1) on the edge of the flat region; (2) on the top surface of the bump; and (3) on the sidewall of the bump. The thermocouples were attached to the surface using silver epoxy and cured for over 24 hours to ensure stable attachment to the block surface before the experiments. All thermocouples were calibrated by an Ultra Precise RTD Sensor (Omega) in a temperature-controlled water bath (Lauda RE 207) before use. The updated experimental configuration is shown in Figure S5.

Similar experimental conditions as those in the initial experiments for the two case studies were achieved when condensation occurred. During the condensation process, the surface temperature of the block T_s was recorded at the three different locations: the edge of the flat region (denoted by $T_{s,f}$), the top surface of the bump (denoted by $T_{s,t}$) and the sidewall of the bump (denoted by $T_{s,s}$).

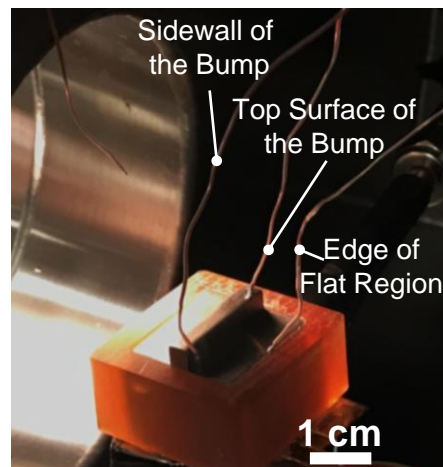


Figure S5. Three thermocouples were attached at different locations on the top surface of the block for direct temperature measurement.

In the case of air-vapor mixture condensation, the steady state condition was obtained at a bulk fluid temperature of 54.3°C with a relative humidity of 85%. For the pure vapor condensation, a steady state at vapor pressure of 5.9 kPa was maintained. The average values from direct temperature measurements for the two cases are listed in Table S2.

Table S2. Experimental conditions and direct temperature measurements

Case	T_{∞} (°C)	Pressure (kPa)	RH(%)	T_b (°C)	$T_{s,f}$ (°C)	$T_{s,t}$ (°C)	$T_{s,s}$ (°C)
Air-Vapor Mixture	54.3	101.3	85.0	12.4	15.3	16.9	16.4
Pure Vapor	35.8	5.9	100.0	22.5	33.9	35.4	35.4

In both cases, the temperature measurement results agree with our model's assumption that the surface temperature of the block T_s should be much closer to the temperature of the element of the thermal resistance network with the much lower resistance (i.e., $(T_s - T_b) \ll (T_{\infty} - T_s)$ in the air-vapor mixture case, where the thermal resistance of the air-vapor mixture dominates, and $(T_s - T_b) \gg (T_{\infty} - T_s)$ in the pure vapor case, where the thermal resistance of the block dominates). In particular, for the pure vapor case, all of the temperatures on the surface of the block were measured to be almost the same as the temperature of the saturated vapor inside the chamber T_{∞} . This observation validated our approximation that $T_s \approx T_{\infty}$ in the pure vapor case. For the air-vapor mixture case, the direct measurement results show that there was a temperature difference of $\sim 4^{\circ}\text{C}$ between T_s and T_b , which could be attributed to two causes. First, the thermocouple measuring T_b was not in perfect contact with the bottom of the block due to the inevitable thermal resistance of the copper tape and the interfacial effects; therefore, the real value of T_b would be higher than the measured value. Second, the conduction and convection effects could decrease the thermal resistance on the gas region side, though these effects were small and thus neglected in our model. Although there was a small temperature change throughout the block, this value was less than one tenth of the temperature difference between the block and the bulk fluid temperature $(T_{\infty} - T_s)$. Therefore, our approximation that $T_s \approx T_b$ in the air-vapor mixture case is justified.

S6. Extended case studies

In this section, we extend our discussion onto more complex thermal resistance scenarios. In order to demonstrate the applicability of the thermal resistance analysis, we exemplify a case study below where we are able to predict the condensation profile through analysis of the thermal resistance network. Our prediction is then validated by numerical calculation results obtained from COMSOL Multiphysics [8].

In this case study, the geometry of the condensation substrate is the same as shown in Figure 1, but the substrate material is changed from titanium to another material with a low thermal conductivity of $k=0.125 \text{ W/(m}\cdot\text{K)}$, such that the thermal resistance of the geometric feature (δ/k) is estimated to be on the same order of magnitude as the thermal resistance of the air-vapor mixture ($1/h$) according to the literature [9, 10]. Therefore, it is no longer valid to assume the condensation substrate is isothermal and to obtain the condensation heat flux by simply solving the concentration profile in the gas region, as we did in the previous air-vapor mixture condensation case study presented in the main text.

The same boundary conditions as the previously considered air-vapor mixture case study are applied: (i) the bottom surface temperature of the condensation block is maintained at a constant $T_b=12^\circ\text{C}$; (ii) the vapor temperature and relative humidity outside the diffusion boundary layer are kept at 56°C and 80%, respectively; and (iii) adiabatic boundary conditions (no heat transfer or mass transfer in the horizontal direction) are applied to the two vertical boundaries of the considered 2D region.

Although it is no longer valid to assume the condensation block to be isothermal, the temperature variation on the top surface of the block is assumed to be small. Therefore, we can still utilize the shape factor method introduced in section S3 to calculate the diffusion boundary layer thickness, which yields the same thickness of 1 cm as calculated previously, since the shape factor method only depends on geometry. Preliminary prediction of the condensation profile can be made by comparing the thermal resistance involved in the characteristic solid region and gas region, as shown in Figure S6.

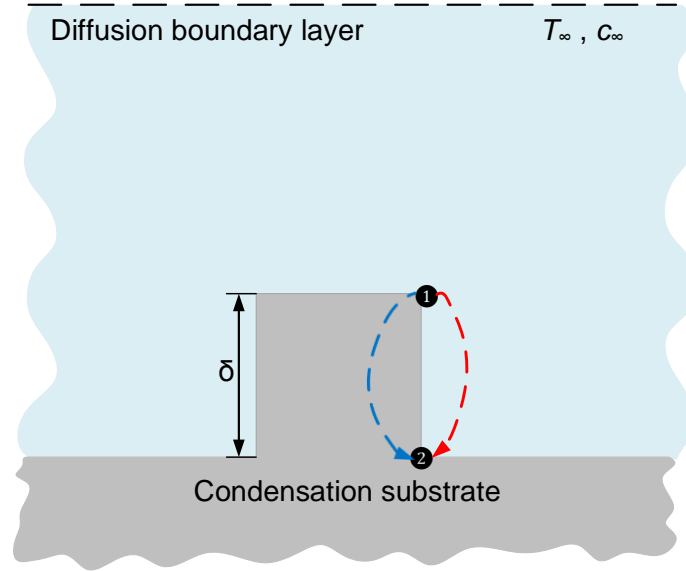


Figure S6. Schematic of the heat and mass transfer process occurring around the geometric feature.

When the heat of the air-vapor mixture reaches position 1, it has two routes to transfer to position 2: (1) through conduction in the solid region, as depicted by the blue dashed line; (2) through mass diffusion and conduction in the gas region, as depicted by the red dashed line. The preferred option of its travel route is determined by the thermal resistance network. For the conduction inside the solid (route (1)), the thermal resistance can be calculated by

$$R_{\text{th, solid}} = \delta / k_{\text{solid}} \cdot \quad (\text{S12})$$

where k_{solid} is the thermal conductivity of the solid substrate (0.125 W/(m·K)).

For the heat and mass transfer in the gas region (route (2)), the total thermal resistance can be calculated by its two paralleled components:

$$R_{\text{th, gas}} = 1 / (1 / R_{\text{th, diff}} + 1 / R_{\text{th, cond}}) \cdot \quad (\text{S13})$$

The first component of the resistance in Equation (S13) accounts for the mass diffusion process, through which latent heat is released at the surface of the substrate:

$$|q| = |j \cdot M \cdot h_{fg}| = \left| D \cdot \frac{\Delta c}{\delta} \cdot M \cdot h_{fg} \right|, \quad (\text{S14})$$

where M denotes the molar mass of water vapor (0.018 kg/mol), D is the diffusion coefficient of vapor in air ($\sim 3.0\text{E-}5 \text{ m}^2/\text{s}$), h_{fg} is the latent heat of water vapor ($\sim 2.4\text{E}6 \text{ J/kg}$) and Δc represents the concentration difference from position 1 to position 2.

According to the definition of thermal resistance per unit area:

$$R_{th} = \Delta T / q, \quad (\text{S15})$$

the thermal resistance caused by the mass diffusion process can be determined as

$$R_{th,diff} = \Delta T / q = \frac{\Delta T}{D \cdot \frac{\Delta c}{\delta} \cdot M \cdot h_{fg}} = \frac{\Delta T}{DMh_{fg}\Delta c} \cdot \delta, \quad (\text{S16})$$

where ΔT represents the temperature difference between position 1 and position 2.

The second component in Equation (S13) represents the thermal resistance due to the conduction effects of the air-vapor mixture, which can be calculated by

$$R_{th,cond} = \delta / k_{gas}, \quad (\text{S17})$$

where k_{gas} denotes the thermal conductivity of the humid air ($\sim 0.026 \text{ W}/(\text{m}\cdot\text{K})$ [11, 12]).

Combining Equations (S12-S17), we can derive the ratio of the thermal resistance of the two routes, denoted by the dimensionless number N :

$$N = \frac{R_{th,diff}}{R_{th,cond}} = \frac{(k_{gas} + \frac{DMh_{fg}\Delta c}{\Delta T})^{-1} \cdot \delta}{\frac{1}{k_{solid}} \cdot \delta} = \frac{k_{solid}}{k_{gas} + \frac{DMh_{fg}\Delta c}{\Delta T}}. \quad (\text{S18})$$

Although the temperature and the corresponding concentration at positions 1 and 2 are unknown, one can derive through a simple scaling that in the considered situation, the value of $\Delta T/\Delta c$ for water near room temperature is on the order of 10. Substituting the values of all of the variables into Equation (S18) yields $N \approx 1$, which predicts that in the current case study, heat has no preference for which route to travel, i.e., heat will transfer from the gas region into the substrate as if the two are the same media. Therefore, the isothermal and iso-concentration lines should be a series of horizontal lines. Consequently, condensation heat flux will almost be the same on the flat regions and the top surface of the bump, since the temperature gradient or concentration gradient in the vertical direction should almost be the same everywhere. However, there will be practically no condensation occurring on the sidewalls of the bump because the concentration gradient or the temperature gradient in the horizontal direction should almost be zero.

In order to demonstrate our prediction from the thermal resistance analysis, we solved the concentration profile in the gas region and the coupled temperature profile in the solid region simultaneously using the COMSOL Multiphysics program. The same boundary conditions at the bottom surface of the substrate and the gas region beyond the diffusion boundary layer as previously mentioned are applied. At the interface of the solid region and the gas region, the conduction heat flux of the solid is balanced by the sum of the conduction heat flux of the humid air and the latent heat flux released by the condensation of the water vapor. Numerical calculation results for the concentration and temperature distribution is shown in Figures S7. Furthermore, the condensation heat flux distribution along the top surface of the condensation substrate is derived from the concentration profile, as shown in Figure S8.

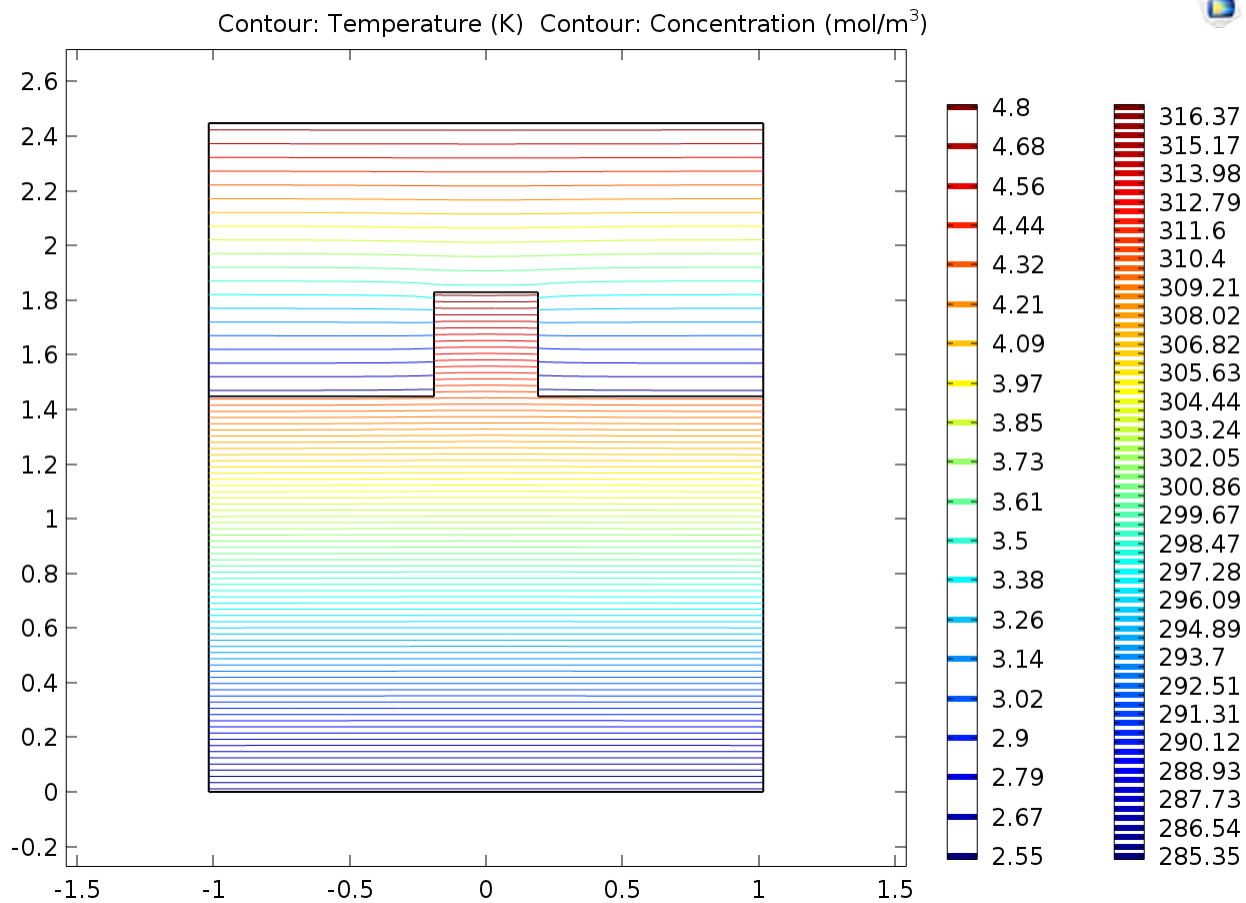


Figure S7. Concentration profile and temperature profile calculated by COMSOL Multiphysics.

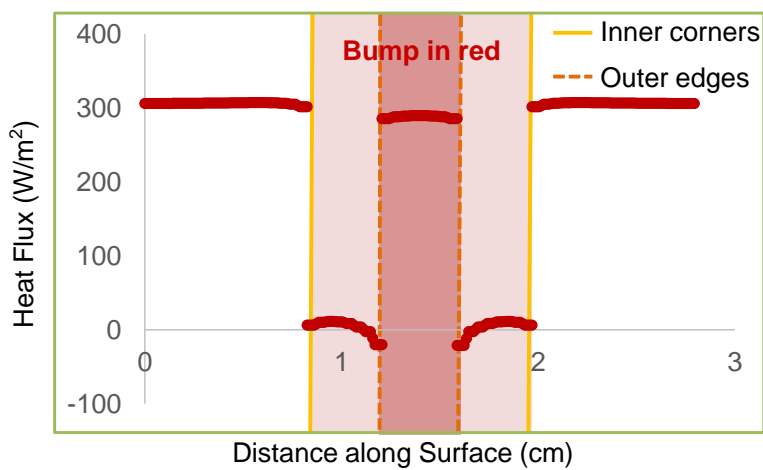


Figure S8. Condensation heat flux distribution along the top condenser surface calculated by COMSOL Multiphysics.

The numerical calculation results shown in Figures S7 and S8 agree with our predictions very well: (1) Temperature and concentration distribute evenly from the upper limit of the diffusion boundary layer to the bottom surface of the condensation substrate, which corresponds to a series of parallel isothermal and iso-concentration lines, respectively, distributed in the solid region and the gas region; (2) Condensation heat flux remains almost constant throughout the horizontal top surfaces of the condensation substrate and drops to nearly zero at the sidewalls of the bump. The relatively low heat flux value in this extended study compared with the two case studies in the manuscript is reasonable, seeing that by changing the thermal conductivity of the block (from 15.6 W/(m·K) to 0.125 W/(m·K)) there was a drastic increase in the overall thermal resistance network. Therefore, it is reliable to predict the condensation profile on a given condenser surface from an analysis on the thermal resistance network even in complex situations where both the heat and mass transfer in the gas region and the heat transfer in the solid region play important roles in the overall heat and mass transfer process.

References for Supplementary Material

- [1] N. Miljkovic, R. Enright, Y. Nam, K. Lopez, N. Dou, J. Sack, E.N. Wang, Jumping-Droplet-Enhanced Condensation on Scalable Superhydrophobic Nanostructured Surfaces, *Nano Lett*, 13(1) (2013) 179-187.
- [2] J.P. Holman, *Heat Transfer*, 10 ed., McGraw-Hill Higher Education, 2009.
- [3] K.C. Park, P. Kim, A. Grinthal, N. He, D. Fox, J.C. Weaver, J. Aizenberg, Condensation on slippery asymmetric bumps, *Nature*, 531(7592) (2016) 78-82.
- [4] D. Beysens, Dew nucleation and growth, *Comptes Rendus Physique*, 7(9-10) (2006) 1082-1100.
- [5] S. Kim, K.J. Kim, Dropwise Condensation Modeling Suitable for Superhydrophobic Surfaces, *Journal of Heat Transfer*, 133(8) (2011) 081502.
- [6] N. Miljkovic, R. Enright, E.N. Wang, Effect of Droplet Morphology on Growth Dynamics and Heat Transfer during Condensation on Superhydrophobic Nanostructured Surfaces_SI, *ACS Nano*, 6 (2012).
- [7] P.B. Weisensee, Y. Wang, Q. Hongliang, D. Schultz, W.P. King, N. Miljkovic, Condensate droplet size distribution on lubricant-infused surfaces, *International Journal of Heat and Mass Transfer*, 109 (2017) 187-199.
- [8] <https://www.comsol.com/comsol-multiphysics>.
- [9] C. Chantana, S. Kumar, Experimental and theoretical investigation of air-steam condensation in a vertical tube at low inlet steam fractions, *Applied Thermal Engineering*, 54(2) (2013) 399-412.
- [10] P. Götze, C. Philipp, U. Gross, Dropwise Condensation Experiments with Humid Air at a Polymer Surface, *Journal of Physics: Conference Series*, 395 (2012) 012129.
- [11] P.T. Tsilingiris, Thermophysical and transport properties of humid air at temperature range between 0 and 100°C, *Energy Conversion and Management*, 49(5) (2008) 1098-1110.
- [12] M.G. Medici, A. Mongruel, L. Royon, D. Beysens, Edge effects on water droplet condensation, *Phys Rev E Stat Nonlin Soft Matter Phys*, 90(6) (2014) 062403.